

# Mass and energy balance calculations for an artificial ice reservoir (Icestupa)

Suryanarayanan Balasubramanian<sup>1,\*</sup>, Martin Hoelzle<sup>1</sup>, Michael Lehning<sup>2</sup>,

Sonam Wangchuk<sup>3</sup>, Johannes Oerlemans<sup>4</sup> and Felix Keller<sup>5</sup>

<sup>1</sup> University of Fribourg, Fribourg, Switzerland

<sup>2</sup> WSL Institute for Snow and Avalanche Research, Davos, Switzerland

<sup>3</sup> Himalayan Institute of Alternatives Ladakh, Leh, India

<sup>4</sup> Institute for Marine and Atmospheric Research, Utrecht University, Utrecht, The Netherlands

<sup>5</sup> Academia Engiadina, Samedan, Switzerland

Correspondence\*:

Suryanarayanan Balasubramanian

suryanarayanan.balasubramanian@unifr.ch

## 2 ABSTRACT

Artificial Ice Reservoirs (AIRs) have been successful in storing water during winter and releasing the water during spring and summer. This has made them a reliable fresh water resource for irrigation in dry environments. Several AIRs have been built but studies of their water storage capacity and efficiency are scarce. This study attempts to model a cone-shaped AIR popularly called Icestupa. Important processes involved in the development and temporal evolution of an Icestupa are calculated by a physically-based model using equations governing the heat transfer, vapour diffusion and transport of water that undergoes phase changes. These processes were quantified using meteorological data in conjunction with fountain spray information (mass input of an Icestupa) to estimate the quantity of frozen, melted, evaporated and runoff water at a location called 'Eispalast' in Fribourg, Switzerland. At this measurement site, an Icestupa was built for model validation purposes. The model was further tested by performing sensitivity and uncertainty study showing that the most sensitive parameters are the ice emissivity and the temperature threshold used to determine precipitation phase. Model calculations estimate that the Eispalast Icestupa stored about 8% of the total water sprayed as ice. In addition, we found that reducing nozzle diameter of the fountain from 5 mm to 3 mm increases the storage efficiency up to 93% without compromising on the storage duration.

Keywords: iceslupa, mass balance, water storage, climate change adaptation, geoengineering

## 1 INTRODUCTION

Seasonal snow cover, glaciers and permafrost are expected to change their water storage capacity due to climate change with major consequences for downriver water supply (Immerzeel et al., 2019). The challenges brought about by these changes are especially important for dry mountain environments such as in Central Asia or the Andes, which directly rely on the seasonal meltwater for their farming and drinking needs (Hoelzle et al., 2019; Apel et al., 2018; Buytaert et al., 2017; Chen et al., 2016; Unger-Shayesteh



**Figure 1.** Icestupa in Ladakh, India on March 2017 was 24 m tall and contained around 3700  $m^3$  of water. Picture Credits: Lobzang Dadul

25 et al., 2013). Some villages in Ladakh, India have already been forced to relocate due to glacial retreat and  
26 the corresponding loss of their main fresh water resources (Grossman, 2015).

27 AIRs have been considered to be a feasible way to adapt to these changes (Hock et al., 2019; Nüsser  
28 et al., 2019b). An artificial ice reservoir is a human-made ice structure typically constructed during the  
29 cold winter months and designed to slowly release freshwater during the warm and dry spring and summer  
30 months. The main purpose of AIRs is irrigation. Therefore, AIRs are designed to store water in the form of  
31 ice as long into the summer as possible. The energy required to construct an AIR is usually derived from  
32 the gravitational head of the source water body. Some are constructed horizontally by freezing water using  
33 a series of checkdams and others are built vertically by spraying water through fountain systems (Nüsser  
34 et al., 2019a). The latter are colloquially referred to as Icestupas and are the subject of this study.

35 A typical Icestupa just requires a pipeline attached to a vertically mounted metal pipe with a fountain  
36 nozzle for construction. Water source is usually a high altitude lake or glacial stream. Due to the altitude  
37 difference between the pipeline input and fountain output, water ejects from the fountain nozzle as droplets  
38 that eventually lose their latent heat to the atmosphere and accumulate as ice around the metal pipe.  
39 The fountain nozzle is raised through addition of further pipes as and when significant ice accumulates.  
40 Typically, a dome of branches is constructed around the metal pipe so that such pipe extensions can be  
41 done from within this dome. During the winter, the fountain is manually activated between sunset and  
42 sunrise. Threads, tree branches and fishing nets are used to guide and accelerate the ice formation.

43 Since their invention in 2013 (Wangchuk, 2014), Icestupas have gained widespread publicity in the region  
44 of Ladakh, Northern India since they require very little infrastructure, skills and energy to be constructed  
45 in comparison to other water storage technologies. Compared to other AIR geometries, Icestupas (Fig.  
46 1) can be built at lower altitudes and last much longer into the summer than other types of ice structures  
47 (Wangchuk, 2014). However, to date, no reliable estimates exist about the amount of sprayed water that  
48 is necessary to create them and the meltwater they provide (Nüsser et al., 2019a). Rough estimates of  
49 Icestupa meltwater in Ladakh suggest that the water loss during the construction process is considerable  
50 (see Appendix 8.1). A complete set of measurements of the water storage and energy balance are required  
51 to understand the cause of the water losses better and increase the construction efficiency.

In this paper, we aim to develop a physically-based model of a vertical AIR (or Icestupa) that can quantify their storage efficiency using existing weather and water usage information. Mass and energy balance equations were used to estimate the quantity of water frozen, melted, evaporated and runoff. Sensitivity and uncertainty analysis were performed to identify the most critical parameters and the variance caused by them. For validation, we created an Icestupa at an accessible site (called Eispalast) near Schwarzsee in the Canton of Fribourg, Switzerland, allowing easy maintenance and control of the measurements. Due to the low altitude of the site with relatively high winter temperatures, only a small Icestupa could be established during winter 2018/19 for providing us with model validation data. Our model and validation experiments provide first steps towards evaluating the effectiveness of a vertical AIR for irrigation and finally we outline some preliminary guidelines for consideration when a construction of an Icestupa for water storage is envisaged.

## 2 STUDY SITE

The Eispalast (EP) site in the Schwarzsee region lies at 967 m a.s.l.. In the winter (Oct-Apr), mean daily maximum and minimum air temperatures vary between 14 to -4 °C. Clear skies are rare, averaging around 7 days, and precipitation amounts average 155 mm per month during winter (Meteoblue, 2020). The site was situated adjacent to a stream resulting in high humidity values across the study period. Within the Eispalast site, 1.8 m in radius enclosure was constructed for the experiment. An automatic weather station (AWS) was set in place adjacent to the wooden boundary as shown in Fig. 2. The fountain used for spraying water had a nozzle diameter of 5 mm and a height of 1.35 m, and was placed in the centre of the wooden enclosure. The water was transferred from a spring water source at 1267 m a.s.l. by pipeline and flowed via a flowmeter and an air escape valve to the nozzle, where it was sprinkled with a spray radius of around 1.7 m. The air escape valve was installed to avoid errors in the flow measurements due to air bubbles. In addition, a webcam guaranteed a continuous survey of the site during the construction of the Icestupa.

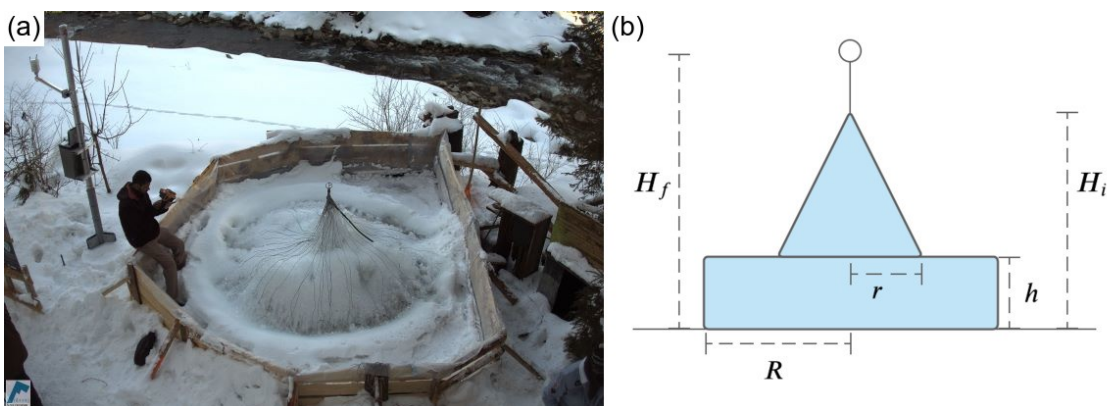


**Figure 2.** (a) The ice structure during the first validation measurement as seen on the webcam image of 14<sup>th</sup> Feb. (b) The corresponding cross section of the EP ice structure with the field estimates of  $r$ ,  $R$ ,  $h$ ,  $H_i$ ,  $H_f$  used to determine the Icestupa volume is shown on the right.

### 2.1 Construction

From 30<sup>th</sup> January to 18<sup>th</sup> March 2019 the Icestupa was constructed through the fountain spray, which was manually switched on if measured air temperature was below -5 °C after sunset and was switched off as soon as the ice was exposed to daylight or temperatures were above 0 °C. The water spray of the fountain was initially adjusted so that most of the water droplets land within the wooden boundary zone. The ice formation was guided by adding a metal framework at the ice structure base after the first night of

80 operation. Several cotton threads were tied between the ice structure base and fountain pole for accelerating  
81 and further guiding the ice formation process.

## 82 2.2 Measurements and Data

83 The EP AWS was located at 967 m a.s.l. It was in operation from 30<sup>th</sup> January to 18<sup>th</sup> March 2019.  
84 Measurements comprise air temperature, relative humidity, water flow rate, wind speed and direction. All  
85 these measurements were stored at a 5 minute sample rate. The water flow rate or discharge was measured  
86 via an ultrasonic sensor attached to the fountain supply pipeline. Precipitation data was derived from the  
87 Plaffeien AWS (IDAWEB, 2019) located 8.8 km away from the measurement site at an altitude of 1042 m  
88 a.s.l.

89 ERA5 reanalysis dataset (Copernicus Climate Change Service (C3S), 2017) correlates much better to  
90 lower elevation sites in Switzerland (Scherrer, 2020). Moreover, all the EP meteorological parameters  
91 except precipitation correlated better with ERA5 dataset compared to the nearby Plaffein AWS. Namely,  
92 the 2 m temperature parameter correlated ( $r^2 = 0.9$ ) with air temperature, surface pressure parameter  
93 correlated ( $r^2 = 1$ ) with air pressure and 10m wind speed parameter (derived from horizontal and vertical  
94 components) correlated ( $r^2 = 0.6$ ) with wind speed. Direct and diffuse shortwave radiation were also  
95 derived from ERA5 surface solar radiation downwards and total sky direct solar radiation parameter. The  
96 hourly ERA5 data and the 10 minute Plaffeien AWS data were linearly interpolated to the 5 minute data  
97 frequency of the EP AWS.

98 Due to a power failure, all data from the EP AWS was lost between 27<sup>th</sup> February 15:20 2019 to 2<sup>nd</sup>  
99 March 15:00 2019. Consequently, the amount of missing data in the dataset was around 7%. During heavy  
100 snowfall events, the ultrasonic wind sensor was blocked and recorded zero values. ERA5 was used to  
101 fill such errors and data gaps . Near-surface humidity is not archived directly in ERA datasets, but from  
102 near-surface (2 m from the surface) temperature ( $T_{ERA5}$ ) and dew point temperature ( $Tw_{ERA5}$ ) one can  
103 calculate relative humidity( $RH$ ) at 2 m as follows:

$$RH = 100 \cdot \frac{e_{sat}(Tw_{ERA5})}{e_{sat}(T_{ERA5})} \quad (1)$$

104 where the saturation vapour pressure function  $e_{sat}$  is expressed with the Teten's formula (Tetens, 1930):

$$e_{sat}(T) = a_1 \cdot e^{(a_3 \cdot \frac{T}{T+273.16-a_4})} \quad (2)$$

105 with T in °C and the parameters set for saturation over water ( $a_1 = 611.21$  Pa,  $a_3 = 17.502$  and  $a_4 = 32.19$   
106 K) according to Buck (1981). Zero wind speed values were recorded whenever snow accumulated on the  
107 ultrasonic wind sensor. So all null values were replaced using the ERA5 dataset.

108 The ERA5 grid point chosen (Latitude 46° 38' 24" N, Longitude 7° 14' 24" E) for the EP site was around  
109 9 km away from the actual site. So all the ERA5 variables were fitted with the Schwarzee dataset via linear  
110 regressions. Through this modified ERA5 dataset, we were also able to further extend the EP dataset and  
111 allow the model to run beyond 18<sup>th</sup> March 2019. Precipitation was filled as null values beyond 18<sup>th</sup> March  
112 2019.

### 113 2.2.1 Field Measurements for validation

114 The volume was determined by decomposing the ice structure into a cylinder (length  $2R$  and height  $h$ )  
115 and a cone (radius  $r$  and height ( $H_i - h$ )) through the following equation:

$$V = \pi \cdot R^2 \cdot h + 1/3 \cdot \pi \cdot r^2 \cdot (H_i - h) \quad (3)$$

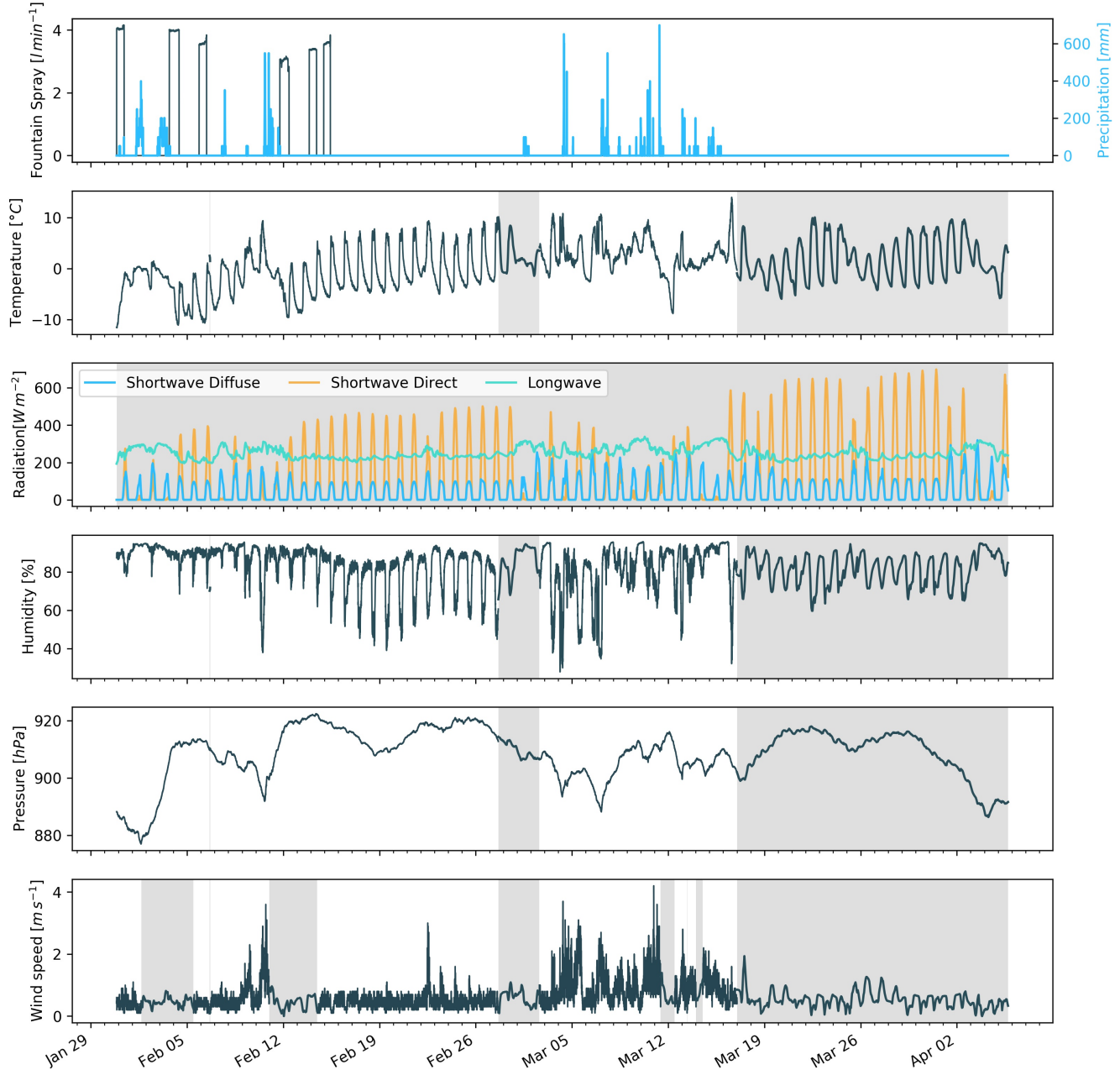


**Figure 3.** Measurements at the AWS of EP were used as main model input data in 5 minute frequency. Plaffeien AWS provided the precipitation data. Incoming shortwave and longwave radiation were obtained from ERA5 reanalysis dataset. Several data gaps and errors were also filled from the ERA5 dataset (shaded regions).

116 Manual measurements were performed at the end of the freezing period on 14<sup>th</sup> February 16:00 2019  
 117 (only one more fountain run was possible after this date) to estimate  $r, R, h, H_i, H_f$  (see Fig. 2 for the  
 118 different geometry components):

$$0.55 \leq r \leq 1\text{m} ; 1.1 \leq R \leq 1.2\text{m} ; 0.1 \leq h \leq 0.2\text{m} ; 0.6 \leq H_i \leq 0.8\text{m} ; 1.3 \leq H_f \leq 1.4\text{m}$$

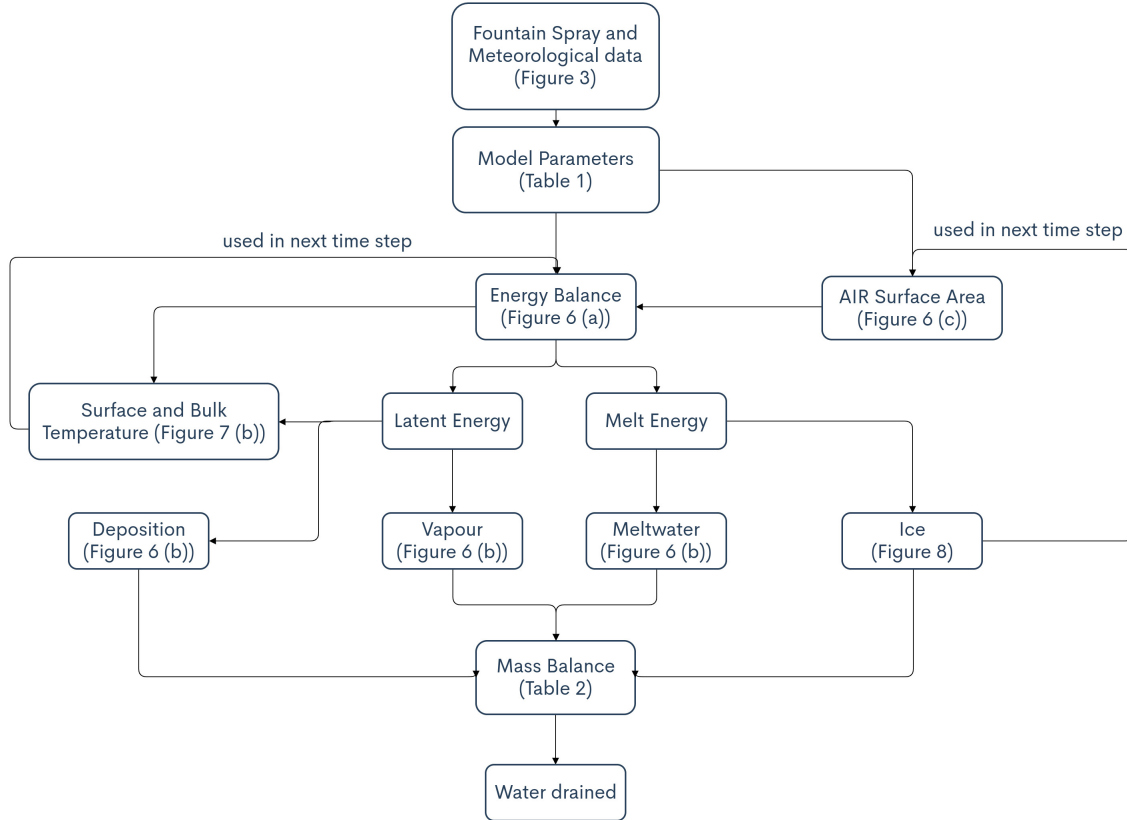


**Figure 4.** Model schematic showing the algorithm used in the model at every time step. Further details about these variables can be found in the associated tables and figures.

119 The ranges of the variables show its variance across different compass orientations. Correspondingly, the  
120 volume range estimated for the first validation point was  $0.857 \pm 0.186 m^3$  on 14<sup>th</sup> February 16:00 2019.

121 The second validation point corresponds to the end of the melting process on 10<sup>th</sup> March 18:00 2019.  
122 Based on the webcam imagery and manual measurement, a thin layer of ice with an observed thickness  
123 between 0.01 to 0.06 m could be quantified. This results in the volume range for the second validation to  
124 be  $0.13 \pm 0.09 m^3$  on 11<sup>th</sup> March 2019

125 In reality, the EP ice structure was more cylindrical until a height of 0.2 m and conical afterwards until a  
126 height of 0.6 m with a radius of 1.18 m. However, we assume a conical shape of this ice structure in order  
127 to apply the modelling strategy described below.

### 3 MODEL SETUP

128 The model (implemented in python) consists of three parts calculating a) the geometric evolution of the  
129 Icestupa, b) the energy balance and c) the mass balance as shown schematically in Fig. 4. A bulk energy  
130 and mass balance model is used to calculate the amounts of ice, liquid water, water vapour and runoff water  
131 of the Icestupa every 5 minutes. The equations used henceforth display model time step superscript only if  
132 it is different from the current time step.

#### 133 3.1 Icestupa geometric evolution

134 Radius  $r_{ice}$  and height  $h_{ice}$  define the dimensions of the Icestupa assuming its geometry to be a cone as  
135 shown in Fig. 5. The surface area  $A$  exposed to the atmosphere and volume  $V$  are:

$$A = \pi \cdot r_{ice} \cdot \sqrt{r_{ice}^2 + h_{ice}^2} \quad (4)$$

$$V = \pi/3 \cdot r_{ice}^2 \cdot h_{ice} \quad (5)$$

136 With the mass of the Icestupa  $M_{ice}$ , its current volume can also be expressed as:

$$V = M_{ice}/\rho_{ice} \quad (6)$$

137 where  $\rho_{ice}$  is the density of ice ( $917 \text{ kg m}^{-3}$ ). The model of the Icestupa is initialised with a thickness  
 138 of  $\Delta x$  (defined in 3.2) and a circular area of radius  $r_F$ . The constant  $r_F$  represents the mean spray radius  
 139 of the fountain. This fountain spray radius is determined by modelling the projectile motion of the water  
 140 droplets. Using mass conservation the droplet speed  $v_F$  can be determined from the spray rate  $d_F$  and the  
 141 diameter  $dia_F$  of the nozzle as follows:

$$v_F = \frac{d_F}{\pi \cdot dia_F^2/4} \quad (7)$$

142 Afterwards, we assume that the water droplets move with an air friction free projectile motion from  
 143 the fountain nozzle with a height  $h_F$  to the ice/ground surface. The resulting spray radius  $r_F$  was then  
 144 determined from the projectile motion equation as follows:

$$r_F = \frac{v_F \cdot \cos\theta_F (v_F \cdot \sin\theta_F + \sqrt{(v_F \cdot \sin\theta_F)^2 + 2 \cdot g \cdot h_F})}{g} \quad (8)$$

145 where  $g = 9.8 \text{ ms}^{-2}$  is the acceleration due to gravity and  $\theta_F = 45^\circ$  is the angle of launch.

146 During subsequent time steps, the dimensions of the Icestupa evolve assuming a uniform ice formation  
 147 and decay across its surface area with an invariant slope  $s_{cone} = \frac{h_{ice}}{r_{ice}}$  as shown in Fig. 5. During these time  
 148 steps, the volume is parameterised using Eqn. 5 as:

$$V = \pi/3 \cdot r_{ice}^3 \cdot s_{cone} \quad (9)$$

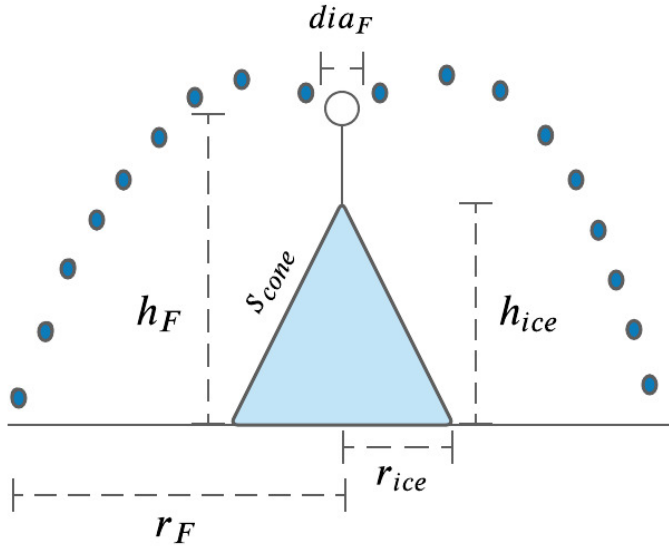


**Figure 5.** Shape and fountain parameters of the EP Icestupa.  $r_{ice}$  is the radius,  $h_{ice}$  is the height and  $s_{cone}$  is the slope of the ice cone.  $r_F$  is the spray radius,  $h_F$  is the height and  $dia_F$  is the nozzle diameter of the fountain.

149 However, the Icestupa cannot outgrow the maximum range of the water droplets ( $(r_{ice})_{max} = r_F$ ).  
 150 Combining equations 5, 6 and 9, the geometric evolution of the Icestupa at each time step  $i$  can be  
 151 determined by considering the following rules:

$$(r_{ice}, h_{ice}) = \begin{cases} (r_F, \Delta x) & \text{if } i = 0 \\ (r_{ice}^{i-1}, \frac{3 \cdot M_{ice}}{\pi \cdot \rho_{ice} \cdot (r_{ice}^{i-1})^2}) & \text{if } r_{ice}^{i-1} \geq r_F \text{ and } \Delta M_{ice} > 0 \text{ where } \Delta M_{ice} = M_{ice}^{i-1} - M_{ice}^{i-2} \\ (\frac{3 \cdot M_{ice}}{\pi \cdot \rho_{ice} \cdot s_{cone}})^{1/3} \cdot (1, s_{cone}) & \text{otherwise} \end{cases} \quad (10)$$

### 152 3.2 Energy Balance

153 The energy balance equation for the Icestupa is formulated as follows:

$$q_{net} = q_{SW} + q_{LW} + q_L + q_S + q_F + q_G \quad (11)$$

154 where  $q_{net}$  is the net energy flux in  $[W m^{-2}]$ ;  $q_{SW}$  is the net shortwave radiation;  $q_{LW}$  is the net longwave  
 155 radiation;  $q_L$  and  $q_S$  are the turbulent latent and sensible heat fluxes.  $q_F$  represents the heat exchange of the  
 156 fountain water droplets with the AIR ice surface during fountain on time steps.  $q_G$  represents ground heat  
 157 flux between Icestupa surface and Icestupa interior. Energy transferred in the direction of the ice surface is  
 158 always denoted as positive and away as negative.

159 Equation 11 is usually referred to as the energy budget for “the surface”, but practically it must apply to a  
 160 surface layer of ice with a finite thickness  $\Delta x$ . The energy flux acts upon the Icestupa surface layer which  
 161 has an upper and a lower boundary defined by the atmosphere and the ice body of the Icestupa, respectively.  
 162 The parameter selection for  $\Delta x$  is based on the following two arguments: (a) the ice thickness  $\Delta x$  should

163 be small enough to represent the daily surface temperature variations and (b)  $\Delta x$  should be large enough  
 164 for these temperature variations to not reach the bottom of the surface layer. Therefore, we introduced a 5  
 165 mm thick ice surface layer, over which the energy balance is calculated. A sensitivity analysis was later  
 166 performed to understand the influence of this factor. Here, we define the surface temperature  $T_{ice}$  to be  
 167 the modelled average temperature of the Icestupa surface layer and the energy flux  $q_{net}$  is assumed to act  
 168 uniformly across the Icestupa area  $A$ .

### 169 3.2.1 Net Shortwave Radiation $q_{SW}$

170 The net shortwave radiation  $q_{SW}$  is computed as follows:

$$171 \quad q_{SW} = (1 - \alpha) \cdot (SW_{direct} \cdot f_{cone} + SW_{diffuse}) \quad (12)$$

171 where  $SW_{direct}$  and  $SW_{diffuse}$  are the ERA5 direct and diffuse short wave radiation,  $\alpha$  is the modelled  
 172 albedo and  $f_{cone}$  is the area fraction of the ice structure exposed to the direct shortwave radiation.

173 We model the albedo using a scheme described in Oerlemans and Knap (1998). The scheme records the  
 174 decay of albedo with time after fresh snow is deposited on the surface.  $\delta t$  records the number of time steps  
 175 after the last snowfall event. After snowfall, albedo changes over a time step,  $\delta t$ , as

$$\alpha = \alpha_{ice} + (\alpha_{snow} - \alpha_{ice}) \cdot e^{(-\delta t)/\tau} \quad (13)$$

176 where  $\alpha_{ice}$  is the bare ice albedo value (0.35),  $\alpha_{snow}$  is the snow ice albedo value (0.85) and  $\tau$  is a decay  
 177 rate, which determines how fast the albedo of the ageing snow reaches this value. The decay rate  $\tau$  is  
 178 assumed to have a base value of 10 days similar to values obtained by Schmidt et al. (2017) for wet surfaces  
 179 and its maximal value is set based on observations by Oerlemans and Knap (1998) as shown in Table 1.  
 180 Furthermore, the albedo  $\alpha$  varies depending on the water source that formed the current Icestupa surface.  
 181 Correspondingly, the albedo is reset to the value of bare ice albedo if the fountain is spraying water onto  
 182 the current ice surface and to the value of fresh snow albedo if a snowfall event occurred. Snowfall events  
 183 are assumed if the air temperature is below  $T_{rain} = 1^{\circ}C$  (Fujita and Ageta, 2000).

184 The area fraction  $f_{cone}$  of the ice structure exposed to the direct shortwave radiation depends on the  
 185 shape considered. The direct solar radiation incident on the AIR surface is first decomposed into horizontal  
 186 and vertical components using the solar elevation angle  $\theta_{sun}$ . For a conical shape, half of the total curved  
 187 surface is exposed to the vertical component of the direct shortwave radiation and the projected triangle  
 188 of the curved surface is exposed to the horizontal component of the direct shortwave radiation. The solar  
 189 elevation angle  $\theta_{sun}$  used is modelled using the parametrisation proposed by Woolf (1968). Accordingly,  
 190  $f_{cone}$  is determined as follows:

$$191 \quad f_{cone} = \frac{(0.5 \cdot r_{ice} \cdot h_{ice}) \cdot \cos\theta_{sun} + (\pi \cdot r_{ice}^2 / 2) \cdot \sin\theta_{sun}}{\pi \cdot r_{ice} \cdot (r_{ice}^2 + h_{ice}^2)^{1/2}} \quad (14)$$

191 The measured diffuse shortwave radiation is assumed to impact the conical Icestupa surface uniformly.

### 192 3.2.2 Net Longwave Radiation $q_{LW}$

193 The net longwave radiation  $q_{LW}$ , for which there were no direct measurements available at EP, is  
 194 determined as follows:

$$q_{LW} = LW_{in} - \sigma \cdot \epsilon_{ice} \cdot (T_{ice} + 273.15)^4 \quad (15)$$

195 where  $T_a$  represents the measured air temperature,  $T_{ice}$  is the modelled surface temperature, both  
 196 temperatures are given in  $^{\circ}\text{C}$ ,  $\sigma = 5.67 \cdot 10^8 \text{ J m}^{-2} \text{ s}^{-1} \text{ K}^{-4}$  is the Stefan-Boltzmann constant,  $LW_{in}$   
 197 denotes the incoming longwave radiation derived from the ERA5 dataset and  $\epsilon_{ice}$  is the corresponding  
 198 emissivity value for the Icestupa surface (see Table 1).

### 199 3.2.3 Turbulent sensible $q_S$ and latent $q_L$ heat fluxes

200 The turbulent sensible  $q_S$  and latent heat  $q_L$  fluxes are computed with the following expressions proposed  
 201 by Garratt (1992):

$$q_S = c_a \cdot \rho_a \cdot p_a / p_{0,a} \cdot \frac{\kappa^2 \cdot v_a \cdot (T_a - T_{ice})}{(\ln \frac{h_{AWS}}{z_{ice}})^2} \quad (16)$$

$$q_L = 0.623 \cdot L_s \cdot \rho_a / p_{0,a} \cdot \frac{\kappa^2 \cdot v_a (p_{v,a} - p_{v,ice})}{(\ln \frac{h_{AWS}}{z_{ice}})^2} \quad (17)$$

202 where  $h_{AWS}$  is the measurement height above the ground surface of the AWS (in  $m$ ),  $v_a$  is the wind  
 203 speed in  $\text{m s}^{-1}$  and  $M_F$  denotes fountain water spray mass in  $\text{kg}$ .  $c_a$  is the specific heat of air at  
 204 constant pressure ( $1010 \text{ J kg}^{-1} \text{ K}^{-1}$ ),  $\rho_a$  is the air density at standard sea level ( $1.29 \text{ kg m}^{-3}$ ),  $p_{0,a}$  is the air  
 205 pressure at standard sea level ( $1013 \text{ hPa}$ ),  $\kappa$  is the von Karman constant (0.4),  $L_s$  is the heat of sublimation  
 206 ( $2848 \text{ kJ kg}^{-1}$ ) and  $z_{ice}$  (1.7 mm) denotes the roughness length of ice (momentum and scalar) described  
 207 in (Garratt, 1992). The vapor pressures over air ( $p_{v,a}$ ) and ice ( $p_{v,ice}$ ) was obtained using the following  
 208 formulation given in WMO (2018):

$$\begin{aligned} p_{v,a} &= 6.107 \cdot 10^{(7.5 \cdot T_a / (T_a + 237.3))} \\ p_{v,ice} &= (1.0016 + 3.15 \cdot 10^{-6} \cdot p_a - 0.074 \cdot p_a^{-1}) \cdot (6.112 \cdot e^{(22.46 \cdot T_{ice} / (T_{ice} + 272.62))}) \end{aligned} \quad (18)$$

209 where  $p_a$  is the measured air pressure in  $\text{hPa}$ .

### 210 3.2.4 Fountain water heat flux $q_F$

211 The total energy flux is further influenced through the heat flux caused by the water that was additionally  
 212 added to the surface of the Icestupa during the time the fountain was running. We take this interaction  
 213 between the fountain water and the ice surface into account by assuming that the ice surface temperature  
 214 stays constantly at  $0^{\circ}\text{C}$  during time steps when the fountain is active. This process can be divided into two  
 215 simultaneous steps: (a) the water temperature  $T_{water}$  is cooled to  $0^{\circ}\text{C}$  and (b) the ice surface temperature is  
 216 warmed to  $0^{\circ}\text{C}$ . Process (a) transfers hereby the necessary energy for process (b) throughout the fountain  
 217 runtime. We further assume that this process is instantaneous, i.e. the ice temperature is immediately set  
 218 to  $0^{\circ}\text{C}$  within just one time step  $\Delta t$  when the fountain is switched on. Thus, the heat flux caused by the  
 219 fountain water is calculated as follows:

$$q_F = \begin{cases} 0 & \text{if } \Delta M_F = 0 \\ \frac{\Delta M_F \cdot c_{water} \cdot T_{water}}{\Delta t \cdot A} + \frac{\rho_{ice} \cdot \Delta x \cdot c_{ice} \cdot T_{ice}}{\Delta t} & \text{if } \Delta M_F > 0 \end{cases} \quad (19)$$

220 with  $c_{ice}$  as the specific heat of ice.

### 221 3.2.5 Bulk Icestupa heat flux $q_G$

222 The bulk Icestupa heat flux  $q_G$  corresponds to the ground heat flux in normal soils and is caused by  
223 the temperature gradient between the surface layer and the ice body. It is expressed by using the heat  
224 conduction equation as follows:

$$225 \quad q_G = k_{ice} \cdot (T_{bulk} - T_{ice}) / l_{ice} \quad (20)$$

226 where  $k_{ice}$  is the thermal conductivity of ice in  $[W m^{-1} K^{-1}]$ ,  $T_{bulk}$  is the mean temperature of the ice  
227 body within the Icestupa and  $l_{ice}$  is the average distance of any point in the surface to any other point in the  
ice body.  $T_{bulk}$  is initialised as  $0^\circ C$  and later determined from Eqn. 20 as follows:

$$228 \quad T_{bulk} = T_{bulk}^{i-1} - (q_G \cdot A \cdot \Delta t) / (M_{ice} \cdot c_{ice}) \quad (21)$$

229 Since we assume a conical shape with  $r_{ice} > h_{ice}$ ,  $l_{ice}$  cannot be greater than  $2r_{ice}$  and also cannot  
230 be less than  $\Delta x$ . Therefore, the average distance from any point on the surface to any point inside is  
 $231 \Delta x \leq l_{ice} \leq r_{ice}$ . We calculate  $q_G$  here assuming  $l_{ice} = r_{ice}/2$ .

### 232 3.2.6 Surface temperature changes and melt energy $q_{melt}$

233 The available net energy  $q_{net}$  partly increases surface temperature, but also contributes to ice melt at the  
234 surface of the Icestupa.  $q_T$  denotes the energy used on changing the surface temperature  $T_{ice}$  and  $q_{melt}$   
denotes the energy used to produce meltwater. So Eqn. 11 can be rewritten as:

$$235 \quad q_{net} = q_{melt} + q_T \quad (22)$$

236 We define the freezing energy as  $q_{freeze} = (q_{net} - q_L)$ . This is because the latent heat always contributes  
237 to temperature fluctuations. Now, the temperature fluctuates based on 3 scenarios namely, (1) the freezing  
238 energy flux is negative but cannot freeze all the fountain water output; (2) the freezing energy flux is  
239 negative and can freeze all the fountain water output; (3) the freezing energy is positive and (4) the fountain  
is inactive ( $\Delta M_F = 0$ ). Therefore, we express the rate of change of temperature as follows:

$$\frac{\Delta T}{\Delta t} = \begin{cases} -T_{ice}^{i-1} / \Delta t & \text{if } q_{freeze} < 0 \text{ and } \Delta M_F \geq -q_{freeze} \cdot A \cdot \Delta t / L_f \\ (\Delta M_F \cdot L_f) / (\rho_{ice} \cdot c_{ice} \cdot \Delta x \cdot A \cdot \Delta t) & \text{if } q_{freeze} < 0 \text{ and } \Delta M_F < -q_{freeze} \cdot A \cdot \Delta t / L_f \\ q_{net} / (\rho_{ice} \cdot c_{ice} \cdot \Delta x) & \text{if } \Delta M_F = 0 \text{ or } q_{freeze} > 0 \end{cases} \quad (23)$$

240 Whenever the model predicts  $T_{ice}^{i+1} > 0^\circ C$ , then the surface temperature is set to  $0^\circ C$  in the corresponding  
241 time step and additional energy contributes to  $q_{melt}$ . Combining these requirements, we get:

$$(q_T, q_{melt}) = \begin{cases} (\rho_{ice} \cdot c_{ice} \cdot \Delta x \cdot \frac{\Delta T}{\Delta t}, q_{net} - q_L - \rho_{ice} \cdot c_{ice} \cdot \Delta x \cdot \frac{\Delta T}{\Delta t}) & \text{if } T_{ice}^{i+1} \leq 0^\circ C \text{ and } \Delta M_F > 0 \\ (\rho_{ice} \cdot c_{ice} \cdot \Delta x \cdot \frac{\Delta T}{\Delta t}, q_{net} - \rho_{ice} \cdot c_{ice} \cdot \Delta x \cdot \frac{\Delta T}{\Delta t}) & \text{if } T_{ice}^{i+1} \leq 0^\circ C \text{ and } \Delta M_F = 0 \\ (-\rho_{ice} \cdot c_{ice} \cdot \Delta x \cdot \frac{T_{ice}^i}{\Delta t}, q_{net} - q_L + \rho_{ice} \cdot c_{ice} \cdot \Delta x \cdot \frac{T_{ice}^i}{\Delta t}) & \text{if } T_{ice}^{i+1} > 0^\circ C \text{ and } \Delta M_F > 0 \\ (-\rho_{ice} \cdot c_{ice} \cdot \Delta x \cdot \frac{T_{ice}^i}{\Delta t}, q_{net} + \rho_{ice} \cdot c_{ice} \cdot \Delta x \cdot \frac{T_{ice}^i}{\Delta t}) & \text{if } T_{ice}^{i+1} > 0^\circ C \text{ and } \Delta M_F = 0 \end{cases} \quad (24)$$

**Table 1.** Free parameters in the model categorised as constant, uncertain and site parameters. Base value (B) and uncertainty (U) were taken from the literature. For assumptions (assum.), the uncertainty was chosen to be relatively large (5 %). For measurements (meas.), the uncertainty due to parallax errors is chosen to be (1 %).

Constant Parameters	Symbol	Value	References
Van Karman constant	$\kappa$	0.4	B: Cuffey and Paterson
Stefan Boltzmann constant	$\sigma$	$5.67 \cdot 10^{-8} W m^{-2} K^{-4}$	B: Cuffey and Paterson
Air pressure at sea level	$p_{0,a}$	1013 hPa	B: Mölg and Hardy
Density of water	$\rho_w$	$1000 kg m^{-3}$	B: Cuffey and Paterson
Density of ice	$\rho_{ice}$	$917 kg m^{-3}$	B: Cuffey and Paterson
Density of air	$\rho_a$	$1.29 kg m^{-3}$	B: Mölg and Hardy
Specific heat of water	$c_w$	$4186 J kg^{-1} ^\circ C^{-1}$	B: Cuffey and Paterson
Specific heat of ice	$c_{ice}$	$2097 J kg^{-1} ^\circ C^{-1}$	B: Cuffey and Paterson
Specific heat of air	$c_a$	$1010 J kg^{-1} ^\circ C^{-1}$	B: Mölg and Hardy
Thermal conductivity of ice	$k_{ice}$	$2.123 W m^{-1} K^{-1}$	B: Bonales et al.
Latent Heat of Sublimation	$L_s$	$2848 kJ kg^{-1}$	B: Cuffey and Paterson
Latent Heat of Evaporation	$L_e$	$2514 kJ kg^{-1}$	B: Cuffey and Paterson
Latent Heat of Fusion	$L_f$	$334 kJ kg^{-1}$	B: Cuffey and Paterson
Gravitational acceleration	$g$	$9.81 m s^{-2}$	B: Cuffey and Paterson
Uncertain Parameters			Range
Precipitation	$T_{rain}$	$1 ^\circ C$	$\pm 1 ^\circ C$
Temperature threshold			B + U: Fujita and Ageta, Zhou et al.
Ice Emissivity	$\epsilon_{ice}$	0.95	$\pm 5 \%$
Ice Albedo	$\alpha_{ice}$	0.35	$\pm 5 \%$
Snow Albedo	$\alpha_{snow}$	0.85	$\pm 5 \%$
Albedo Decay Rate	$\tau$	10 days	[1, 22] days
Ice layer thickness	$\Delta x$	5 mm	[1, 10] mm
Site Parameters			
Fountain diameter	nozzle	$dia_F$	5 mm
Fountain height		$h_F$	$\pm 1 \%$
Fountain temperature	water	$T_{water}$	$1.35 m$
AWS height		$h_{AWS}$	$5 ^\circ C$
			[0, 9] °C
			$\pm 1 \%$
			B: meas. ; U: assum.
			B: meas. ; U: assum.
			B: meas. ; U: meas.
			B: meas. ; U: assum.

### 242 3.3 Mass Balance

243 The mass balance equation is used to derive the water that drains away  $M_{runoff}$  as follows:

$$\frac{\Delta M_{runoff}}{\Delta t} = \frac{\Delta M_F + \Delta M_{ppt} + \Delta M_{dpt} - \Delta M_{ice} - \Delta M_{melt} - \Delta M_{vapour}}{\Delta t} \quad (25)$$

244 where  $\Delta M = M^i - M^{i-1}$ . Here  $\frac{\Delta M_F}{\Delta t} = d_F$  where  $d_F$  is the spray of the fountain measured in  $[kg s^{-1}]$ ;  
 245  $M_{ppt}$  is the cumulative precipitation and  $M_{dpt}$  is the cumulative accumulation through water vapour  
 246 condensation or deposition;  $M_{ice}$  is the cumulative mass of ice;  $M_{melt}$  is the cumulative mass of melt water  
 247 and  $M_{vapour}$  represents the cumulative water vapor loss by evaporation or sublimation.

248 Precipitation input is calculated as:

$$\frac{\Delta M_{ppt}}{\Delta t} = \begin{cases} \pi \cdot r_{ice}^2 \cdot \rho_w \cdot ppt & \text{if } T_a < T_{rain} \\ 0 & \text{if } T_a \geq T_{rain} \end{cases} \quad (26)$$

249 where  $\rho_w$  is the density of water ( $1000 kg m^{-3}$ ),  $ppt$  is the measured precipitation rate in  $[m s^{-1}]$  and  
 250  $T_{rain}$  is the temperature threshold below which precipitation falls as snow. Here, snowfall events were  
 251 identified using  $T_{rain}$  as  $1^\circ C$ . Snow mass input is calculated by assuming a uniform deposition over the  
 252 entire circular footprint of the Icestupa.

253 The latent heat flux is used to estimate either the evaporation and condensation processes or sublimation  
 254 and deposition processes. To differentiate between these two possibilities, we classify the time steps into  
 255 humid or non-humid if the corresponding relative humidity value is above or below 60 % (Stigter et al.,  
 256 2018). On humid time steps we assume condensation or evaporation to occur whereas on non-humid time  
 257 steps deposition or sublimation can occur. Correspondingly, latent heat of evaporation ( $L_e$ ) is used for  
 258 humid time steps and latent heat of sublimation ( $L_s$ ) is used for non-humid time steps. Water accumulation  
 259 and vapour loss from the Icestupa surface is calculated as follows:

$$\left( \frac{\Delta M_{vapour}}{\Delta t}, \frac{\Delta M_{dpt}}{\Delta t} \right) = \begin{cases} (-q_L \cdot A/L, 0) & \text{if } q_L < 0 \\ (0, q_L \cdot A/L) & \text{if } q_L \geq 0 \end{cases} \quad (27)$$

260 where  $L = \begin{cases} L_s & \text{if } RH < 60 \\ L_e & \text{if } RH \geq 60 \end{cases}$

261 Using the melt energy  $q_{melt}$ , we estimate the frozen and melted ice mass ( $\Delta M_{ice}$ ,  $\Delta M_{melt}$ ). Removing  
 262 the contribution of precipitation and combining Eqn. 27 we are left with the contribution from the melt  
 263 energy as follows:

**Table 2.** Summary of calculated mass balance components for the EP experiment after the fountain spray was stopped on 15<sup>th</sup> February 2019 and at the end of the model run on 5<sup>th</sup> April.

	Mass Component	Fountain spray ends	Model ends
Input	$M_F$	18060 kg	18060 kg
	$M_{ppt}$	444 kg	467 kg
	$M_{dpt}$	7 kg	33 kg
Output	$M_{melt}$	165 kg	1023 kg
	$M_{ice}$	814 kg	0 kg
	$M_{vapour}$ $M_{runoff}$	3 kg 17529 kg	8 kg 17529 kg

$$\left( \frac{\Delta M_{ice} - \Delta M_{ppt} - \Delta M_{dpt} + \Delta M_{vapour}}{\Delta t}, \frac{\Delta M_{melt}}{\Delta t} \right) \text{ if } RH < 60 \\ \left( \frac{\Delta M_{ice} - \Delta M_{ppt} - \Delta M_{dpt}}{\Delta t}, \frac{\Delta M_{melt} + \Delta M_{vapour}}{\Delta t} \right) \text{ if } RH \geq 60 \right\} = \begin{cases} \frac{q_{melt} \cdot A}{L_f} \cdot (-1, 1) & \text{if } q_{melt} \geq 0 \\ \frac{q_{melt} \cdot A}{L_f} \cdot (-1, 0) & \text{if } q_{melt} < 0 \text{ and } \frac{\Delta M_F}{\Delta t} \geq -\frac{q_{melt} \cdot A}{L_f} \\ \left( \frac{\Delta M_F}{\Delta t}, 0 \right) & \text{if } q_{melt} < 0 \text{ and } 0 \leq \frac{\Delta M_F}{\Delta t} < -\frac{q_{melt} \cdot A}{L_f} \end{cases} \quad (28)$$

- 264 Now, with all the other terms known in Eqn. 25, the water drainage/runoff can now be determined.  
 265 Considering AIRs as water reservoirs, we can quantify their potential through the amount of water they  
 266 store (storage quantity) and the length of time they store it (storage duration). Another means of comparing  
 267 different Icestupas is through their water storage efficiency defined accordingly as:

$$\text{Storage Efficiency} = \frac{M_{melt}}{(M_F + M_{ppt} + M_{dpt})} \cdot 100 \quad (29)$$

## 4 MODEL RESULTS

- 268 The model was forced with meteorological data from 30<sup>th</sup> January to 5<sup>th</sup> April 2019 (Fig. 3) and various  
 269 parameters (see Table 1) to calculate the mass and energy balance of the Icestupa.

### 4.1 Energy and mass balance calculation

- 271 Daily averages of some components of the energy balance are shown in Fig. 6 (a). On average during the  
 272 experiment duration, the total energy flux between the atmosphere and the Icestupa are almost balanced.  
 273 Net shortwave radiation ( $28 \text{ W m}^{-2}$ ), sensible ( $17 \text{ W m}^{-2}$ ) and latent heat flux ( $9 \text{ W m}^{-2}$ ) with a mostly  
 274 positive flux towards the surface of the icestupa are compensated by the net longwave radiation (- 36  
 275  $\text{W m}^{-2}$ ) and the melt energy (-19  $\text{W m}^{-2}$ ). The contribution of other fluxes are negligible in comparison.

- 276 Net shortwave radiation is the main input to, and the most varying energy flux on the ice surface. Its  
 277 variability is controlled by the surface albedo  $\alpha$  and the area fraction  $f_{cone}$  which therefore represent key  
 278 variables in the energy balance (Fig. 7 (a)). Although global radiation flux reached a daily maximum

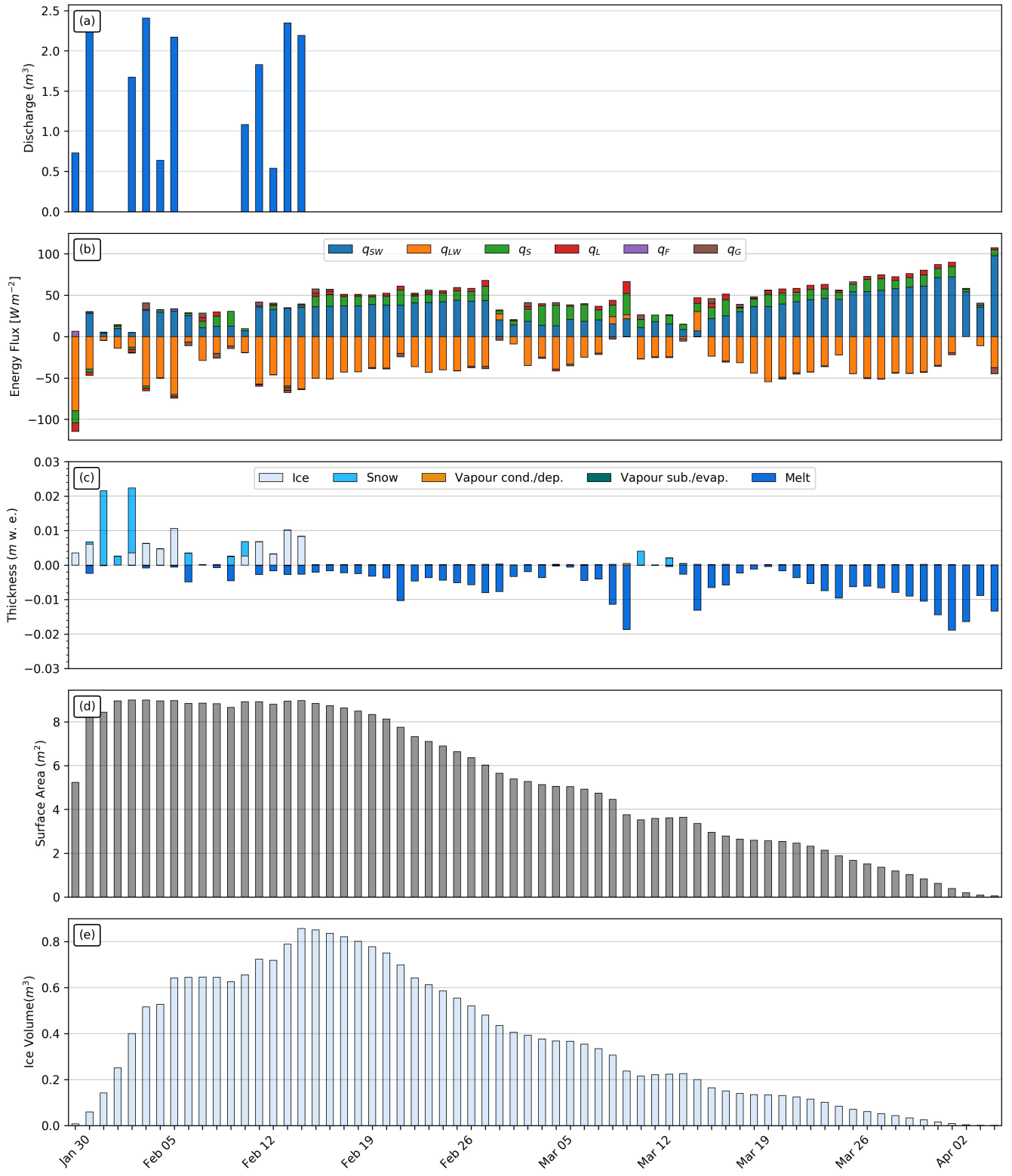


**Figure 6.** (a) Fountain discharge (b) energy flux components, (c) mass flux components (d) surface area and (e) volume of the Icestupa in daily time steps.  $q_{SW}$  is the net shortwave radiation;  $q_{LW}$  is the net longwave radiation;  $q_L$  and  $q_S$  are the turbulent latent and sensible heat fluxes.  $q_F$  represents the interactions of the ice-water boundary during fountain on time steps.  $q_G$  quantifies the heat conduction process between the Icestupa surface layer and the ice body.

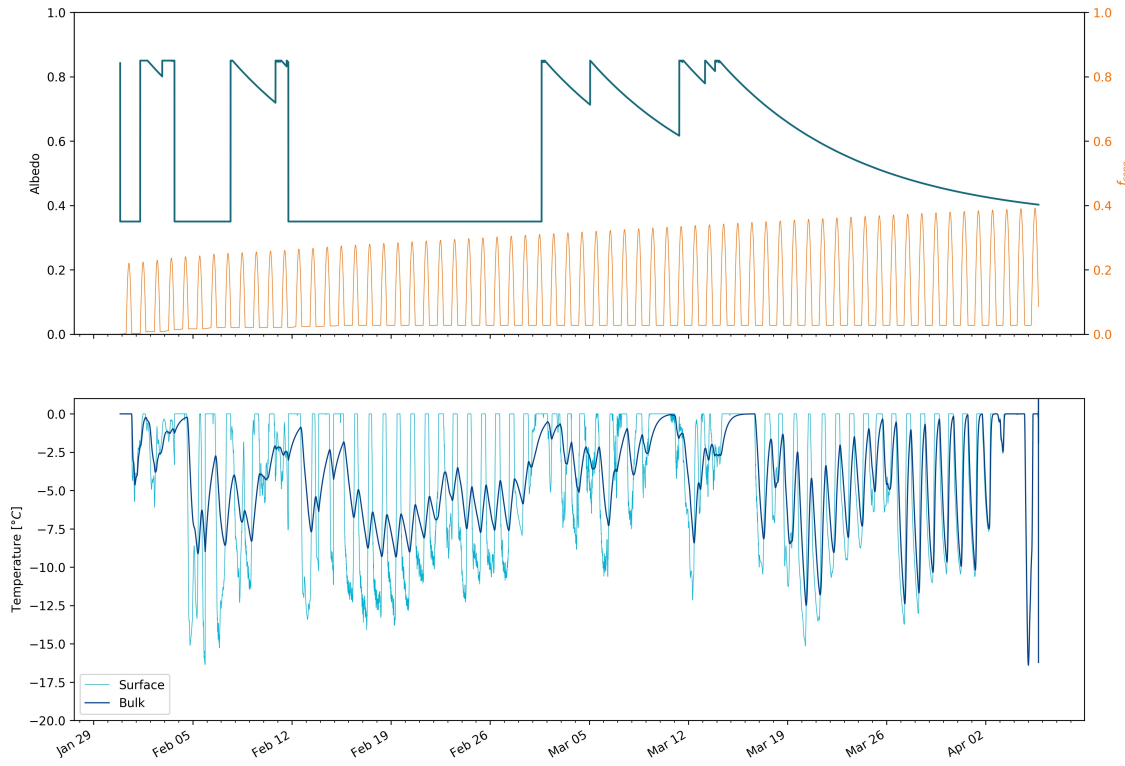


**Figure 7.** Some derived parameters of the model, namely, albedo and  $f_{cone}$  (a), Surface and bulk temperature (b). In (a), the black curve shows how snow and fountain-on events reset albedo between ice albedo and snow albedo. The decay of the snow albedo to ice albedo can also be observed. The blue curve shows how the solar radiation area fraction varied diurnally with variations in the solar elevation angle. In (b), the surface temperature (black curve) was forced to be  $0\text{ }^{\circ}\text{C}$  during fountain activity. The corresponding bulk temperature is shown with the blue curve.

279 value of  $304\text{ }Wm^{-2}$ ,  $q_{SW}$  only went up to  $68\text{ }Wm^{-2}$ . This is caused by the fact that only about 30 % of  
 280 the direct solar radiation influenced the Icestupa surface as shown by the area fraction  $f_{cone}$  in Fig. 7 (a).  
 281 Snowfall is the atmospheric variable connected most closely and proportionally to albedo. Higher and/or  
 282 more frequent snowfall thus decreases the energy available for melt due to the corresponding increase in  $\alpha$ .

283  $q_{LW}$  was predominantly negative indicating that this energy balance component drove the freezing of the  
 284 ice structure. The incoming longwave radiation was strongly dependent on atmospheric emissivity which  
 285 had a mean value of 0.77. Atmospheric emissivity in turn depended on the cloudiness factor. Daily values  
 286 of  $q_{LW}$  ranged from -95 to  $7\text{ }Wm^{-2}$ .  $q_{LW}$  and  $q_S$  were both proportional to the temperature gradient  
 287 between the air and the Icestupa surface. Turbulent sensible heat flux  $q_S$  contributed mostly to the melt  
 288 of the ice structure. Daily values of  $q_S$  ranged from -16 to  $59\text{ }Wm^{-2}$ . Turbulent latent heat flux  $q_L$  was  
 289 predominantly positive suggesting that it favoured deposition/condensation over evaporation/sublimation.  
 290 Daily values of  $q_L$  ranged from -4 to  $47\text{ }Wm^{-2}$ . Therefore, the Icestupa gained mass cumulatively from  
 291 the atmosphere due to the deposition/condensation process. Fountain water heat flux  $q_F$  had a mean of  
 292 zero as it was only nonzero during 1002 time steps or around 100 hours. Daily values of  $q_F$  ranged from  
 293 0 to  $7\text{ }Wm^{-2}$ . The contribution of heat flux by conduction  $q_G$  was minimal as it only varied between  
 294 -7 to  $7\text{ }Wm^{-2}$  with a mean of  $0\text{ }Wm^{-2}$ . The energy contributing to surface temperature changes ( $q_T$ )  
 295 was insignificant in comparison to the energy spent on freezing and melting ( $q_{melt}$ ). The resulting bulk  
 296 temperature and the surface temperature are shown in Fig. 7 (b). For the total considered period,  $q_{LW}$

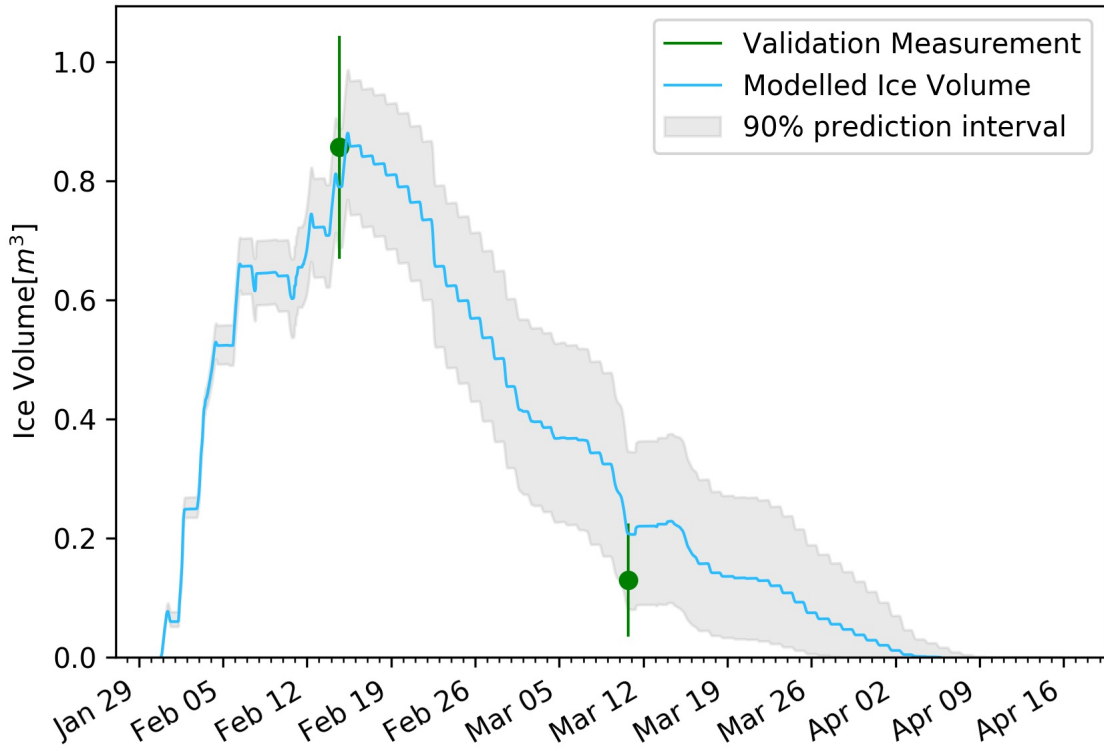


**Figure 8.** Modelled ice volume during the lifetime of the EP Icestupa (blue curve). Green line segments indicate the first and second validation measurements. The prediction interval is based on the ice volume uncertainty caused by the most sensitive parameters, namely, temperature threshold below which precipitation falls as snow and the ice emissivity.

297 accounted for 28.3% of overall energy turnover. The energy turnover is calculated as the sum of energy  
 298 fluxes in absolute values.  $q_{SW}$  accounted for 21.7%, followed by  $q_{melt}$  (25.4%),  $q_S$  (14.6%),  $q_L$  (7.5%),  $q_G$   
 299 (1.8%),  $q_F$  (0.3%) and  $q_T$  (0.3%).

300 Fig. 6 (b) represents the mass fluxes associated with these energy exchanges expressed in  $m$  w.e. It  
 301 shows the ice and meltwater formed due to  $q_{melt}$ , snow accumulated due to precipitation, water vapour  
 302 deposition/condensation and sublimation/evaporation due to  $q_L$ . Growth rate ( $\frac{\Delta M_{ice}}{\Delta t}$ ) shows a strong  
 303 correlation with net energy flux ( $r^2 = 0.44$ ) but poor correlation with Icestupa surface area ( $r^2 = 0.04$ ).  
 304 This is because the variance in growth rate is mostly due to the variance in  $q_{net}$  as illustrated in Fig. 6.  
 305 Since  $r_{ice}$  was initialised with the spray radius  $r_F$ , the surface area maintains a maximum initially until the  
 306 energy flux becomes positive. This trend favours the positive over the negative thickness changes resulting  
 307 in a steep increase and gradual melting of ice volume as can be seen in Fig. 8.

308 The total water used for the Icestupa development includes contributions from the fountain (97.2%),  
 309 snowfall (2.5 %) and deposition/condensation (0.3 %) as shown in Table 2. The maximum ice mass during  
 310 the whole measurement period was 1158 kg, which occurred after the last fountain run on Feb 16<sup>th</sup> in  
 311 the morning. Therefore, in the case of EP we used a water input of 18,584 kg, with a resultant storage  
 312 efficiency of only 7.5 %.

## 5 MODEL SENSITIVITY AND UNCERTAINTY ANALYSIS

313 The icestupa model can be regarded as a function  $f(x_1, x_2 \dots, x_n) = (y_1, y_2 \dots, y_m)$ , where  
 314  $(x_1, x_2 \dots, x_n)$  are the model parameters and  $(y_1, y_2 \dots, y_m)$  are the model outputs. The influence of each  
 315 parameter on the output variables of interest were quantified and the most important physical parameters  
 316 for the subsequent uncertainty analysis were determined. The sensitivity of a parameter  $x_j$  is determined  
 317 by keeping all other parameters  $x_i, i \neq j$  fixed at their baseline value and varying  $x_j$  within values that are  
 318 physically plausible.

319 A sensitivity study on the parameters (listed in Table 1) was performed with the maximum ice volume  
 320 as the target variable. All the parameters were assumed to be independent of each other with a uniform  
 321 distribution. This assumption ignores the auto-correlation present among the parameters associated with  
 322 the albedo parameterisation. The range of uncertain parameters were set based on available literature values  
 323 or varied  $\pm 5\%$  from the base value if no such reference was available. The uncertainty of all the site  
 324 parameters were caused due to parallax errors during manual measurement. This was quantified with a  
 325 range of  $\pm 1\%$  from the base value. However, it must be kept in mind that, even though intended to be as  
 326 objective as possible, the selection of a parameter range has a subjective part that influences the results and  
 327 conclusions obtained in this analysis. The variation of the model outputs  $y_k$  is evaluated to quantify the  
 328 local sensitivities  $s_{j,k}$  that are defined here as the 95% range of the simulated outputs.

329 To perform the uncertainty analysis, we included only parameters that influence the maximum ice volume  
 330 by at least  $0.1 m^3$ . All other parameters were fixed at their baseline value. Fig. 9 shows all the variance  
 331 produced by these uncertain parameters in maximum ice volume calculation. It shows that  $\epsilon_{ice}$  and  $T_{rain}$   
 332 are the only parameters with a maximal sensitivity of more than  $0.1 m^3$  for the maximum ice volume  
 333 estimate. Consequently, all other parameters were excluded from the subsequent uncertainty analysis.

334 The temperature threshold below which precipitation falls as snow ( $T_{rain}$ ) was found to be the most  
 335 sensitive parameter. It is used in the model to reset the albedo to snow albedo and determine snow  
 336 precipitation events. The lower  $T_{rain}$  parameter the higher the albedo (as the Icestupa surface has a lower  
 337 albedo when ice-covered than when snow-covered). The variation of  $T_{rain}$  by  $\pm 1^\circ C$  caused maximum  
 338 ice volume variation of  $1.2 \pm 0.2 m^3$ .

339 Ice emissivity was also found to be a sensitive parameter. The higher the ice emissivity the larger the  
 340 maximum ice volume as the emitted longwave radiation increases with ice emissivity. Variation of  $\epsilon_{ice}$  by  
 341 5% caused a maximum ice volume range from  $1.3 \pm 0.1 m^3$ .

342 In total, the sensitivity analysis required 120 simulations, and the uncertainty analysis a total of 32  
 343 simulations.

## 6 DISCUSSION

### 344 6.1 Model validation quality

345 We first evaluate the model against the validation measurements at the EP site. The uncalibrated model is  
 346 able to capture both the freezing and the melting process sufficiently well as the modelled ice volume lies  
 347 within the uncertainty of both validation measurements. Furthermore, the validation measurements fit well  
 348 within the estimated model uncertainty. However, since this validation is based on only two points, it does  
 349 limit the confidence in the model results. Moreover, the model seems to overestimate the ice volume at  
 350 both validation points. This could be due to the underestimation of the surface area which underestimates  
 351 the melt rates (absolute growth rate when  $\frac{\Delta M_F}{\Delta t} < 0$ ) and the freeze rates (absolute growth rate when  
 352  $\frac{\Delta M_F}{\Delta t} > 0$ ). However, as the fountain was mostly inactive during the study period, the underestimation

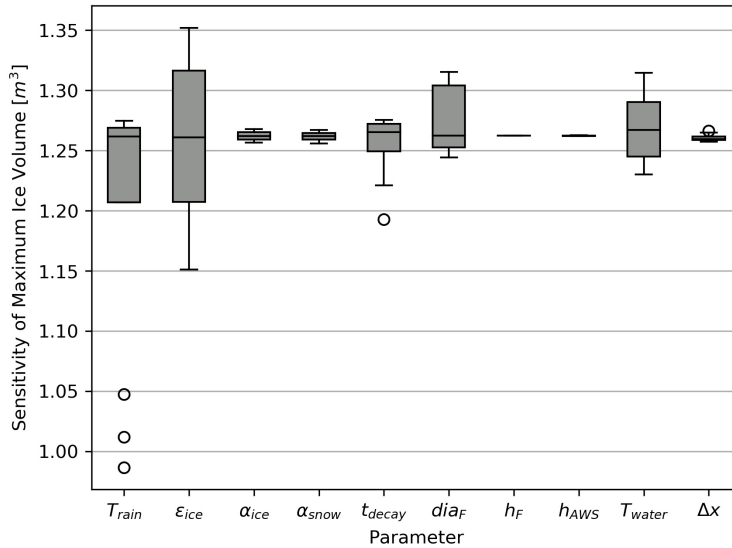


**Figure 9.** Sensitivities of maximum ice volume to all the uncertain and site parameters used in the model (Table 1). Outliers in the bar plot are shown as 'o'.

of surface area disproportionately undervalues the melt rates over the freeze rates. One major cause of this underestimation was the conical shape assumption, as in reality, the Icestupa shape ranged between a cone and a cylinder (Fig. 2). Another cause was the surface irregularities that were observed due to uneven exposure to direct solar radiation and fountain droplets. The sensitivity of the model results to these errors was further amplified due to the relatively small volume of the EP Icestupa. In summary, more validation measurements on a more voluminous Icestupa would have increased confidence on the model results.

## 6.2 Important assumptions

In the sensitivity and uncertainty analysis presented above, we did not account for several general assumptions and parametrisation choices that may cause model errors. Some assumptions and their potential to cause errors are discussed below.

- Turbulent Sensible and Latent Heat Fluxes: The method used to calculate the turbulent heat fluxes by Garratt (1992) assumes that the turbulent heat fluxes are acting over a uniform planar surface to determine the roughness length. Since our application is on a conical surface, the distance to the ice surface is not uniform and well defined. Hence,  $z_{ice}$  has no real physical significance here.
- Droplet flight time loss: Water losses during the flight time of fountain droplets were neglected making all the fountain spray available for freezing. For the EP experiment, inclusion of this parameter does not influence results since it is already accounted for in the runoff water discharge rate which was at least  $3 l min^{-1}$ .
- Nucleation of droplets: Corresponding to droplet flight time, ice/snow formation is also possible before surface contact if nucleation occurs during flight time. For the EP experiment, this process will further increase the freeze rate and hence the storage efficiency. This process is neglected for model simplicity.

## 6.3 Schwarzsee vs Leh Icestupa

It could be argued that the relatively small EP Icestupa cannot be compared with the much larger Icestupas in Ladakh which store millions of litres of water for several months (see Appendix 8.1). However, this is the only Icestupa dataset available for such a model validation.

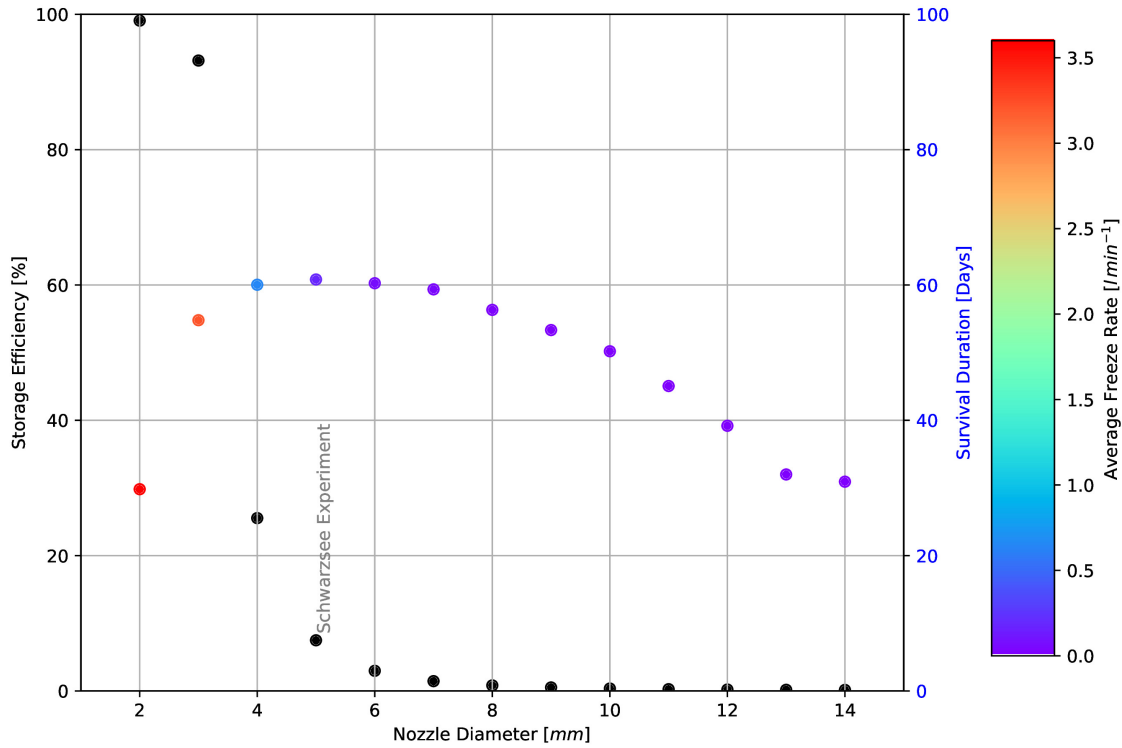


**Figure 10.** Variation in storage efficiency (black dots) and storage duration (coloured dots) with changes in fountain nozzle's nozzle diameter. The dot colours represent average freeze rate based on the color bar.

378 Table 2 clearly shows that for our EP experiment most of the input water (92 %) simply runoff away.  
 379 This high water loss through drainage is due to the fact that the average spray rate of the fountain  
 380 ( $(\frac{\Delta M_F}{\Delta t})_{mean} = 3.6 \text{ l min}^{-1}$ ) far exceeded the max Icestupa growth rate ( $(\frac{\Delta M_{ice}}{\Delta t})_{max} = 1 \text{ l min}^{-1}$  (w.e.) ).

381 In the city of Leh, Ladakh at an altitude of 3500 m a.s.l. the air temperature shows values down to 27.9  
 382 °C in winter (Chevuturi et al., 2018) whereas EP had a minimum temperature of just -11.6 °C during the  
 383 study period. Moreover, subzero temperatures were only reached for 7 nights of fountain operation at the  
 384 EP site compared to the 43 nights of fountain operation possible in Ladakh (see Appendix 8.1). Thus,  
 385 the Icestupa growth rate is expected to be much higher in Ladakh. However, water spray rates in Ladakh  
 386 are also much higher (around  $210 \text{ l min}^{-1}$ ). So the water losses in Ladakh could also be caused due to  
 387 excessive fountain spray.

#### 388 6.4 Icestupa construction decisions

389 There are several decisions one has to take when constructing Icestupas. These can be broadly divided  
 390 into two types of decisions, namely fountain and location decisions. Both the meteorological conditions  
 391 of the location and the surface area produced by the fountain significantly influence the observed growth  
 392 rate. Since our validation is restricted to just one location, we restrict our discussion to the optimization  
 393 possibilities of Icestupa constructions through fountain decisions.

394 Assuming a constant spray for the fountain, we can divide the fountain decisions into fountain state  
 395 (on/off) and type (height and nozzle diameter). From an energy balance point of view, the fountain should  
 396 be switched on for all time intervals when  $q_{net} < 0$ . However, in our experiment, the fountain state decision  
 397 was set based on whether the ambient temperature was above or below a critical temperature of -5°C.  
 398 Ambient temperature can serve as an indicator of  $q_{net}$  as it was correlated ( $r^2 = 0.53$ ). However,  $q_{net}$

399 was found to be negative already at a critical temperature of  $-1^{\circ}\text{C}$ . Therefore, using air temperature to  
400 determine when the fountain should be switched on is justified but a higher critical temperature could have  
401 been used in the case of the EP Icestupa.

402 The fountain type used can be characterised by the physical structure of the fountain, namely its height and  
403 nozzle diameter. Maintaining the same spray rate and height, one can optimize the Icestupa development  
404 by identifying the minimum nozzle diameter that yields the maximum storage efficiency.

405 Fig. 10 shows reducing the nozzle diameter to  $3\text{ mm}$  increases storage efficiency up to 93 % without  
406 compromising much on storage duration. The corresponding storage quantity of the  $3\text{ mm}$  nozzle diameter  
407 was more than 20 times higher than the  $5\text{ mm}$  fountain used in our experiment. This is because the spray  
408 radius  $r_F$  of the  $3\text{ mm}$  fountain was much higher at  $8.5\text{ m}$  compared to the  $1.7\text{ m}$  spray radius of the  
409  $5\text{ mm}$  fountain (see Appendix Section ??). Here, we define growth rate as freeze rate when fountain is  
410 active and melt rate otherwise. So this higher spray radius both, increases the freeze rate and increases  
411 the melt rate since they are both directly proportional to the surface area. However, since the freeze rate  
412 cannot increase beyond a spray rate of  $3.6\text{ l min}^{-1}$  (except during precipitation or deposition/condensation  
413 events), an optimum spray radius or nozzle diameter exists, beyond which storage duration suffers due to a  
414 disproportionate increase in melt rate compared to the freeze rate. So even though  $3\text{ mm}$  nozzle diameter  
415 had a much higher storage quantity than the  $5\text{ mm}$  nozzle, its storage duration was around 6 days less than  
416 the  $5\text{ mm}$  nozzle. One physical cause of this effect is the different shapes of both the ice structures. A flat  
417 sheet of ice (effectively a cone with a high spray radius) with higher mass might have a storage duration  
418 shorter than a conical ice structure. As the spray radius decreases with increasing nozzle diameter, the ice  
419 structure's average slope increases and so the  $5\text{ mm}$  nozzle's ice structure is "more" conical than the  $3\text{ mm}$   
420 ice structure. Fig. 10 shows that a nozzle diameter of  $3\text{ mm}$  has an average freeze rate ( $3.2\text{ l min}^{-1}\text{w.e.}$ )  
421 which is large enough to increase the storage efficiency and small enough to not reduce the storage duration  
422 of the Icestupa significantly.

## 7 CONCLUSIONS

423 We outlined a methodology for estimating ice, liquid water, water vapour and runoff quantities produced  
424 during the construction of an Icestupa using measurements of fountain spray rate, air temperature, radiation,  
425 humidity, pressure, wind and cloudiness at the EP study site. The comparison with validation measurements  
426 at two different dates during the experiment led to satisfying results, although a more rigorous model  
427 validation was not possible due to few icestupa volume measurements.

428 According to the model, the EP Icestupa achieved a storage quantity of 1392 litres of water with a  
429 storage duration of 61 days. However, the corresponding storage efficiency was very low with only 7.5 %  
430 for a water input of 18,584 litres. These estimates were most sensitive to the temperature threshold that  
431 determined precipitation phase and ice emissivity parameters which created an uncertainty of  $1.2 \pm 0.3\text{ m}^3$   
432 in the maximum ice volume calculated. This is to be expected as net longwave radiation and net shortwave  
433 radiation together accounted for around 50 % of the overall energy turnover.

434 Although the location, storage quantity and duration of our experimental EP Icestupa are not representative  
435 of the much larger Icestupas of Ladakh, the model results do support the hypothesis that there could be  
436 considerable water loss during the formation of Icestupas particularly due to excessive fountain spray.  
437 Using model calculations, it was shown that a decreased fountain nozzle diameter of  $3\text{ mm}$  can increase the  
438 storage efficiency drastically. This is because a change in the fountain nozzle diameter causes an effective  
439 change of the ice surface area over which the net energy flux can act. This result has relevance on the future  
440 design of Icestupa fountains. However, care has to be taken as our model is currently only validated by one

441 experiment at the EP site. Further experiments at different locations with different fountains are required to  
442 better understand the influence of construction decisions on the results.

## 8 APPENDIX

### 443 8.1 Ladakh Icestupa 2014/15

444 A 20 m tall Icestupa (Wangchuk, 2015c) was built in Phyang village, Ladakh at an altitude of 3500  
445 m a.s.l. Assuming a conical shape with a diameter of 20 m, the corresponding volume of this Icestupa  
446 becomes  $2093 \text{ m}^3$  or 1,919,587 litres w.e. The fountain sprayed water at a rate of  $210 \text{ l min}^{-1}$  (Wangchuk,  
447 2015e) from 21<sup>st</sup> January (Wangchuk, 2015a) to at least until 5<sup>th</sup> March 2015 (Wangchuk, 2015b) (around  
448 43 nights). Assuming fountain spray was active for 8 hours each night, we estimate water consumption to  
449 be around 4,334,400 litres. So just during construction/freezing period of the Icestupa, roughly 56 % of the  
450 water provided was wasted. The actual water loss is bound to be much higher due to further vapour losses  
451 during the melting period. This Icestupa completely melted away on 6<sup>th</sup> July 2015 (Wangchuk, 2015d).  
452 Therefore, the storage duration was 166 days or roughly 5 months.

## CONFLICT OF INTEREST STATEMENT

453 The authors declare that the research was conducted in the absence of any commercial or financial  
454 relationships that could be construed as a potential conflict of interest.

## AUTHOR CONTRIBUTIONS

455 SB wrote the initial version of the manuscript. MH, ML, SW, JO, and FK commented on the initial  
456 manuscript and helped improve it. SB developed the methodology with inputs from MH. SB performed the  
457 analysis with support from MH and ML. SB and MH participated in the fieldwork.

## FUNDING

458 This work was supported and funded by the University of Fribourg and by the Swiss Government Excellence  
459 Scholarship (Suryanarayanan Balasubramanian).

## ACKNOWLEDGMENTS

460 We thank Mr. Adolf Kaeser and Mr. Flavio Catillaz at Eispalast Schwarzsee for their active participation  
461 in the fieldwork. We would also like to thank Digmesa AG for subsidising their flowmeter used in the  
462 experiment. We would particularly like to thank the editor Prof. Thomas Schuler who gave us important  
463 inputs to improve the paper and we thank also Prof. Christian Hauck and Prof. Nanna B. Karlsson for  
464 valuable suggestions that improved the manuscript.

## DATA AVAILABILITY STATEMENT

465 The data and code used to produce results and figures will be published at a later stage and can, until then,  
466 be obtained from the authors upon request.

## REFERENCES

- 467 Apel, H., Abdykerimova, Z., Agalhanova, M., Baimaganbetov, A., Gavrilenko, N., Gerlitz, L., et al. (2018).  
468 Statistical forecast of seasonal discharge in central asia using observational records: development of a  
469 generic linear modelling tool for operational water resource management. *Hydrology and Earth System  
470 Sciences* 22, 2225–2254. doi:10.5194/hess-22-2225-2018

- 471 Bonales, L. J., Rodriguez, A. C., and Sanz, P. D. (2017). Thermal conductivity of ice prepared under  
472 different conditions. *International Journal of Food Properties* 20, 610–619. doi:10.1080/10942912.  
473 2017.1306551
- 474 Buck, A. L. (1981). New equations for computing vapor pressure and enhancement factor. *Journal of  
475 Applied Meteorology and Climatology* 20, 1527 – 1532
- 476 Buytaert, W., Moulds, S., Acosta, L., Bievre, B. D., Olmos, C., Villacis, M., et al. (2017). Glacial melt  
477 content of water use in the tropical andes. *Environmental Research Letters* 12, 114014. doi:10.1088/  
478 1748-9326/aa926c
- 479 Chen, Y., Li, W., Deng, H., Fang, G., and Li, Z. (2016). Changes in central asia's water tower: Past, present  
480 and future. *Nature* doi:10.1088/1748-9326/aa926c
- 481 Chevuturi, A., Dimri, A. P., and Thayyen, R. J. (2018). Climate change over leh (ladakh), india. *Theoretical  
482 and Applied Climatology* 131, 531–545. doi:10.1007/s00704-016-1989-1
- 483 [Dataset] Copernicus Climate Change Service (C3S) (2017). Era5: Fifth generation of ecmwf atmospheric  
484 reanalyses of the global climate
- 485 Cuffey, K. M. and Paterson, W. S. B. (2010). *The Physics Of Glaciers* (Elsevier)
- 486 Fujita, K. and Ageta, Y. (2000). Effect of summer accumulation on glacier mass balance on the  
487 tibetan plateau revealed by mass-balance model. *Journal of Glaciology* 46, 244–252. doi:10.3189/  
488 172756500781832945
- 489 Garratt, J. R. (1992). *The Atmospheric Boundary Layer* (Cambridge University Press)
- 490 Grossman, D. (2015). As himalayan glaciers melt, two towns face the fallout
- 491 Hock, R., Rasul, G., Adler, C., Cáceres, B., Gruber, S., Hirabayashi, Y., et al. (2019). 2019: High mountain  
492 areas. *IPCC Special Report on the Ocean and Cryosphere in a Changing Climate* [H.-O. Pörtner, D.C.  
493 Roberts, V. Masson-Delmotte, P. Zhai, M. Tignor, E. Poloczanska, K. Mintenbeck, A. Alegria, M. Nicolai,  
494 A. Okem, J. Petzold, B. Rama, N.M. Weyer (eds.)]
- 495 Hoelzle, M., Barandun, M., Bolch, T., Fiddes, J., Gafurov, A., Muccione, V., et al. (2019). *The status and  
496 role of the alpine cryosphere in Central Asia*. doi:10.4324/9780429436475-8
- 497 [Dataset] IDAWEB (2019). Meteoswiss, federal office of meteorology and climatology
- 498 Immerzeel, W. W., Lutz, A. F., Andrade, M., Bahl, A., Biemans, H., Bolch, T., et al. (2019). Importance  
499 and vulnerability of the world's water towers. *Nature* 577, 364 – 369. doi:10.1038/s41586-019-1822-y
- 500 Meteoblue (2020). Climate schwarzsee
- 501 Mölg, T. and Hardy, D. R. (2004). Ablation and associated energy balance of a horizontal glacier surface  
502 on kilimanjaro. *J. Geophys. Res.-Atmos.* 109, 1–13. doi:10.1029/2003JD004338
- 503 Nüsser, M., Dame, J., Kraus, B., Baghel, R., and Schmidt, S. (2019a). Socio-hydrology of artificial glaciers  
504 in ladakh, india: assessing adaptive strategies in a changing cryosphere. *Regional Environmental Change*  
505 doi:10.1007/s10113-018-1372-0
- 506 Nüsser, M., Dame, J., Parveen, S., Kraus, B., Baghel, R., and Schmidt, S. (2019b). Cryosphere-Fed  
507 Irrigation Networks in the Northwestern Himalaya: Precarious Livelihoods and Adaptation Strategies  
508 Under the Impact of Climate Change. *Mountain Research and Development* 39. doi:10.1659/  
509 MRD-JOURNAL-D-18-00072.1
- 510 Oerlemans, J. and Knap, W. H. (1998). A 1 year record of global radiation and albedo in the  
511 ablation zone of morteratschgletscher, switzerland. *Journal of Glaciology* 44, 231–238. doi:10.  
512 3189/S0022143000002574
- 513 Scherrer, S. C. (2020). Temperature monitoring in mountain regions using reanalyses: lessons from the  
514 alps. *Environmental Research Letters* 15, 044005. doi:10.1088/1748-9326/ab702d

- 515 Schmidt, L. S., Aðalgeirs Þóttir, G., Guðmundsson, S., Langen, P. L., Pálsson, F., Mottram, R., et al. (2017).  
516 The importance of accurate glacier albedo for estimates of surface mass balance on vatnajökull: evaluating  
517 the surface energy budget in a regional climate model with automatic weather station observations. *The  
518 Cryosphere* 11, 1665–1684. doi:10.5194/tc-11-1665-2017
- 519 Stigter, E. E., Litt, M., Steiner, J. F., Bonekamp, P. N. J., Shea, J. M., Bierkens, M. F. P., et al. (2018).  
520 The importance of snow sublimation on a himalayan glacier. *Frontiers in Earth Science* 6, 108.  
521 doi:10.3389/feart.2018.00108
- 522 Tetens, O. (1930). Über einige meteorologische begriffe. z. *Geophys.* 6, 297–309
- 523 Unger-Shayesteh, K., Vorogushyn, S., Farinotti, D., Gafurov, A., Duethmann, D., Mandychev, A., et al.  
524 (2013). What do we know about past changes in the water cycle of central asian headwaters? a review.  
525 *Global and Planetary Change* 110, 4 – 25. doi:10.1016/j.gloplacha.2013.02.004. Water in Central Asia  
526 – Perspectives under global change
- 527 Wangchuk, S. (2014). Ice stupa artificial glaciers of ladakh
- 528 Wangchuk, S. (2015a). The good news at ice stupa 24th january 2015
- 529 Wangchuk, S. (2015b). Ice stupa artificial glacier inaugurated 5th of march 2015
- 530 Wangchuk, S. (2015c). Ice stupa surpasses guiness world record
- 531 Wangchuk, S. (2015d). Ice stupa way of celebrating a special day
- 532 Wangchuk, S. (2015e). World water day at ice stupa
- 533 WMO (2018). *Guide to Instruments and Methods of Observation* (World Meteorological Organization ;  
534 2018 (2018 Edition))
- 535 Woolf, H. M. (1968). *On the Computation of Solar Elevation Angles and the determination of sunrise and  
536 sunset times* (National Aeronautics and Space Administration)
- 537 Zhou, S., Kang, S., Gao, T., and Zhang, G. (2010). Response of zhadang glacier runoff in nam co basin,  
538 tibet, to changes in air temperature and precipitation form. *Chinese Science Bulletin* 55, 2103–2110.  
539 doi:10.1007/s11434-010-3290-5